Title

Isogeometric Fatigue Damage Prediction in Large-Scale Composite Structures Driven by Dynamic Sensor Data

Journal

Journal of Applied Mechanics, Transactions ASME, 82(9)

ISSN

0021-8936

Authors

Bazilevs, Y

Deng, X

Korobenko, A

et al.

Publication Date

2015-09-01

DOI

10.1115/1.4030795

Peer reviewed

Y. Bazilevs
Department of Structural Engineering,
University of California–San Diego,
La Jolla, CA 92093
e-mail: yuri@ucsd.edu

X. Deng
Department of Structural Engineering,
University of California–San Diego,
La Jolla, CA 92093

A. Korobenko
Department of Structural Engineering,
University of California–San Diego,
La Jolla, CA 92093

F. Lanza di Scalea
Department of Structural Engineering,
University of California–San Diego,
La Jolla, CA 92093

M. D. Todd
Department of Structural Engineering,
University of California–San Diego,
La Jolla, CA 92093

S. G. Taylor
Los Alamos National Laboratory,
Los Alamos, NM 87545

Isogeometric Fatigue Damage Prediction in Large-Scale Composite Structures Driven by Dynamic Sensor Data

In this paper, we combine recent developments in modeling of fatigue-damage, isogeometric analysis (IGA) of thin-shell structures, and structural health monitoring (SHM) to develop a computational steering framework for fatigue-damage prediction in full-scale laminated composite structures. The main constituents of the proposed framework are described in detail, and the framework is deployed in the context of an actual fatigue test of a full-scale wind-turbine blade structure. The results indicate that using an advanced computational model informed by in situ SHM data leads to accurate prediction of the damage zone formation, damage progression, and eventual failure of the structure. Although the blade fatigue simulation was driven by test data obtained prior to the computation, the proposed computational steering framework may be deployed concurrently with structures undergoing fatigue loading. [DOI: 10.1115/1.4030795]

Keywords: fatigue damage, DDDAS, IGA, Kirchhoff–Love shells, digital twin

1 Introduction

Dynamic data-driven application system (DDDAS) [1] is a framework in which sensor and measurement data collected for a given physical system are used to dynamically update a computational model of that system. Using measurement data, the computational model geometry, boundary conditions, forcing, and material parameters may be updated to better represent physical reality. At the same time, the properly updated computational model is able to produce higher-fidelity outputs for the quantities of interest for which measurements are not readily available. As such, DDDAS is a framework in which measurement and simulation coexist in a symbiotic environment that is very well suited for executing a SHM strategy. SHM is a general process of making an assessment, based on appropriate analyses of in situ measured data, about the current ability of a structural component or system to perform its intended design function(s) successfully. Damage prognosis (DP) extends this process by considering how the SHM state assessment, when combined with future loading (often probabilistic) and failure mode models, may be used to forecast remaining useful life or similar performance-level variables in a way that facilitates efficient life cycle management. It is the focus of this paper to use a DDDAS architecture to demonstrate DP capability by exploiting recent developments in geometric modeling, computational mechanics, high-performance computing (HPC), and measured SHM features applied specifically for a class of medium-to-large-scale laminated composite structures [2]. Computational steering enables one, through monitoring of structures, to detect the onset of damage (defined in this work as local degradation of stiffness) due to external loading, track its evolution, and, eventually, predict structural failure. Furthermore, given the ability to detect and track damage, one may utilize control strategies to shelter structural systems from excessive loading, thereby increasing their chances of survival and prolonging their useful life span.

High-fidelity simulation of medium-to-large-scale structures requires significant computational resources and necessitates utilization of HPC. Unless reduced-order modeling [3,4] is employed, the computations are often time-consuming. As a result, the use of advanced structural mechanics simulation in connection with real-time monitoring of structures and decision making is not common. However, when it comes to fatigue damage, "real-time" no longer presents a daunting task since fatigue damage, in practice, evolves over years or decades, while the corresponding full-scale (or even partial-scale) lab tests take weeks or, in some cases, months to complete. As a result, it is no longer impractical to have a high-fidelity structural model that incorporates fatigue damage and presents a fairly complete digital counterpart of the actual structural system of interest. This observation motivates the main subject of this paper—development of a computational steering framework for fatigue-damage prediction in structures comprised of thin-shell laminated fiber-reinforced composites.

Fatigue of fiber-reinforced composites exhibits complex behavior [5]. A three-stage stiffness degradation can be observed for fiber-reinforced composites: During the first stage, damage initiates within a few hundred loading cycles, with sharp decline of initial stiffness and formation of a damage zone. The second stage is characterized by a gradual loss of stiffness and redistribution of the stress. The third stage typically involves fiber fracture and delamination, leading to accelerated decline of stiffness. Reference [6] presents an account of fatigue modeling challenges in composites. Failure is a multiscale process occurring across different spatial scales, from atomistic to full structure level. Anisotropy in the composite material at the mesoscale level gives rise to

Contributed by the Applied Mechanics Division of ASME for publication in the JOURNAL OF APPLIED MECHANICS. Manuscript received April 16, 2015; final manuscript received June 4, 2015; published online June 25, 2015. Assoc. Editor: Chad M. Landis.

different damage modes, which are often coupled [7]. Accurate characterization of the material properties from its microstructure also presents significant challenges [8–10].

Fatigue modeling and lifetime prediction methodologies for fiber-reinforced composites typically fall into three categories [5,11]: (1) Fatigue life models that use S–N curves or Goodman-type diagrams do not account for the actual damage mechanisms or introduce fatigue failure criteria to determine the specimen fatigue life; (2) phenomenological models for the residual strength and stiffness; and (3) "mechanistic" progressive models use damage variables related to measurable quantities, such as size of matrix cracks. In the present work, we adapt a fatigue-damage model recently proposed in Refs. [12] and [13], which falls in the latter category, and which is able to quantitatively account for progression of damage in complex-geometry composite structures.

The paper is organized as follows. In Secs. 2 and 3, we present the core constituents of our DDDAS framework. In particular, in Sec. 2 we introduce IGA in the context of rotation-free Kirchhoff–Love shell models [14–19] that are suitable for describing thin-laminated composite structures [20,21]. IGA is viewed as one of the key ingredients of the proposed DDDAS framework because it enables seamless integration between structural geometry modeling and computational analysis, both achieved by means of utilizing the same underlying spline-basis-function technology stemming from computer-aided design (CAD). In Sec. 3, we present the fatigue-damage model for fiber-reinforced composites suitable for modeling fully reversed cyclic loading scenarios [12,13] and validate it using a composite-plate bending-fatigue test data. To integrate the damage evolution equations, a "cycle jump" technique is employed, which enhances the overall computational efficiency of the proposed DDDAS framework. In Sec. 4, we focus on the deployment of our DDDAS fatigue-damage framework using a full-scale CX-100 wind-turbine blade designed by Sandia National Laboratories. The CX-100 blade was instrumented with an SHM system comprised of accelerometers and strain gauges, and fatigue-tested to failure at the National Renewable Energy Laboratory [22–25]. We construct a detailed IGA representation of the aforementioned blade and take advantage of the rich accelerometer and strain-gauge data to computationally steer the blade to failure. This computation illustrates that when using an appropriate combination of advanced modeling and dynamic sensor and measurement data, one can obtain highly accurate prediction of local damage initiation and evolution in full-scale structures. In Sec. 5, we draw conclusions and outline future research directions.

2 Isogeometric Analysis of Thin Shell Composite Structures

We start with a description of IGA, which presents a core structural modeling platform in this work. IGA is a recently introduced finite element method (FEM)-like simulation methodology that relies on the geometry representation of CAD, computer graphics, and animation [26–28]. In IGA, the geometry and computational solution fields are represented using the same functional description. The most widely used discretization in IGA makes use of nonuniform rational B-splines (NURBS) [29], but other alternatives, such as T-splines [30,31], are currently being developed and routinely used. As a result of this choice, integration of structural design and computational analysis is greatly simplified. This single representation of the geometry and solution fields allows a direct interaction with as-build geometry, which is needed at different stages of modeling and simulation. IGA is an inherently higher-order accurate technique, and, in addition, the basis functions in IGA are of higher-order continuity than standard FEM. This additional smoothness property is a distinguishing feature of IGA and is beneficial in many applications of computational mechanics (see, e.g., Ref. [27]).

Aerospace and civil composite structures of interest in this work, such as aircraft fuselage, wings, and wind-turbine blades, are geometrically complex, curved thin shells. As a result, to simulate such structures at full scale and with sufficient geometric detail, discretization of thin-shell theories is employed for computational efficiency and is a key to structural modeling of laminated composites. Isogeometric shell analysis was recently proposed in Ref. [16] to address the shortcomings of standard finite-element technology for thin shells. It was found that higher-order continuity (C^1 and above) of the IGA basis functions significantly improved the per-degree-of-freedom accuracy and robustness of thin-shell discretizations as compared to the FEM. Furthermore, the increased continuity of IGA discretizations enabled the use of shell kinematics without rotational degrees of freedom and the development of a new class of Kirchhoff–Love shell formulations [14,15,17], leading to further computational cost savings associated with the analysis of thin structures. The isogeometric rotation-free Kirchhoff–Love shell formulation was successfully applied in the context of fluid–structure interaction modeling of wind turbines in Refs. [20], [21], [32], and [33]. In what follows, we present the basics of the thin-shell formulation employed in this work.

The rotation-free Kirchhoff–Love shell variational formulation may be stated as follows: Find the shell midsurface displacement $\mathbf{y}^h$, such that $\forall \mathbf{w}^h$

$$\begin{aligned}&\int_{\Gamma_0^s} \mathbf{w}^h \cdot \rho_0 h_{th}\left(\frac{\mathrm{d}^2\mathbf{y}^h}{\mathrm{d}t^2} - \mathbf{f}^h\right)\mathrm{d}\Gamma \\ &+ \int_{\Gamma_0^s} \delta\bar{\boldsymbol{\varepsilon}}^h \cdot (\mathbf{A}\bar{\boldsymbol{\varepsilon}}^h + \mathbf{B}\bar{\boldsymbol{\kappa}}^h)\mathrm{d}\Gamma \\ &+ \int_{\Gamma_0^s} \delta\bar{\boldsymbol{\kappa}}^h \cdot (\mathbf{B}\bar{\boldsymbol{\varepsilon}}^h + \mathbf{D}\bar{\boldsymbol{\kappa}}^h)\mathrm{d}\Gamma \\ &+ \int_{\Gamma_0^b} \delta\bar{\boldsymbol{\kappa}}^h \cdot \mathbf{D}^b\bar{\boldsymbol{\kappa}}^h\mathrm{d}\Gamma - \int_{(\Gamma_t^s)_h} \mathbf{w}^h \cdot \mathbf{h}^h\mathrm{d}\Gamma = 0\end{aligned} \tag{1}$$

In the above formulation, Γ_0^s and Γ_t^s are the shell midsurface in the reference and deformed configuration, respectively, $\bar{\boldsymbol{\varepsilon}}$ and $\bar{\boldsymbol{\kappa}}$ are the vectors of membrane-strain and curvature-change coefficients, respectively, in the local coordinate system, ρ is the through-thickness-averaged density, $\delta\bar{\boldsymbol{\varepsilon}}^h$ and $\delta\bar{\boldsymbol{\kappa}}^h$ are the variations of the membrane-strain and curvatures-change vectors, respectively, $(\Gamma_t^s)^h$ is the shell subdomain with a prescribed traction boundary condition, and $\mathbf{h}^h$ is the prescribed traction vector. Furthermore, Γ_0^b denotes the so-called bending-strip domain, which is a key construct of the bending-strip method developed in Ref. [15]. The latter technique allows direct application of rotation-free Kirchhoff–Love shell formulation to geometrically complex structures comprised of multiple surface patches, including nonmanifold situations. To model a composite shell, the classical laminated plate theory [34] is employed. We denote the thickness of the kth ply by t_k and its centroid by $\bar{z}_k$ (see Fig. 1). With these definitions, in Eq. (1), the extensional, coupling, and bending

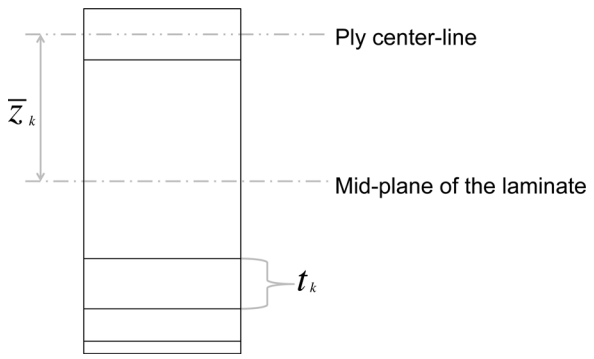

Fig. 1 Composite layup with nonuniform and nonsymmetric distribution of the lamina

stiffnesses, given by **A**, **B**, and **D** matrices, respectively, may be computed for any layup as

$$\mathbf{A} = \int_{h_{th}} \mathbf{C} d\xi_3 = \sum_{k=1}^{n} \overline{\mathbf{C}}_k t_k \tag{2}$$

$$\mathbf{B} = \int_{h_{th}} \xi_3 \overline{\mathbf{C}} d\xi_3 = \sum_{k=1}^{n} \overline{\mathbf{C}}_k t_k \overline{z_k} \tag{3}$$

$$\mathbf{D} = \int_{h_{th}} \xi_3^2 \overline{\mathbf{C}} d\xi_3 = \sum_{k=1}^{n} \overline{\mathbf{C}}_k \left(t_k \overline{z_k^2} + \frac{t_k^3}{12} \right) \tag{4}$$

Here, $\overline{\mathbf{C}}_k$ is a constitutive material matrix for the kth ply in the local coordinate system given by

$$\overline{\mathbf{C}}_k = \mathbf{T}^{\mathrm{T}}(\phi_k) \tilde{\mathbf{C}}_k \mathbf{T}(\phi_k) \tag{5}$$

$$\mathbf{T}(\phi) = \begin{bmatrix} \cos^2\phi & \sin^2\phi & \sin\phi\cos\phi \\ \sin^2\phi & \cos^2\phi & -\sin\phi\cos\phi \\ -2\sin\phi\cos\phi & 2\sin\phi\cos\phi & \cos^2\phi - \sin^2\phi \end{bmatrix} \tag{6}$$

where ϕ denotes the fiber orientation angle in the ply, and $\tilde{\mathbf{C}}$ is the constitutive matrix for the orthotropic material written with respect to the principal material axes (or lamina axes) of the ply (see Ref. [15] for more details).

The present thin-shell formulation is suitable in the regime of large displacements because the strain measures $\bar{\boldsymbol{\varepsilon}}$ and $\bar{\boldsymbol{\kappa}}$ are derived from the Green–Lagrange strain and, as a result, are insensitive to rigid-body translation and rotation. The St. Venant–Kirchhoff material constitutive law is assumed in the above developments. The details of the constitutive matrix $\tilde{\mathbf{C}}$ for the case of fatigue damage are shown in the next section. The Kirchhoff–Love shell equations are discretized in the Galerkin framework using smooth spline functions (NURBS or T-splines) and are integrated in time using the generalized-α method [35].

3 Fatigue Damage Model of Fiber-Reinforced Composites Under Fully Reversed Cyclic Loading

A progressive damage model for fiber-reinforced composite lamina under fully reversed cyclic loading, recently proposed in Ref. [12], is briefly described in this section. The model, which is empirical in nature, is based on continuum damage mechanics and residual stiffness approaches. It is aimed at describing the three stages of local (i.e., at a point in 3D continuum) material stiffness degradation—the initial fast decline in stiffness, followed by the gradual stiffness reduction, and, eventually, complete material failure. In the constitutive model, in the lamina coordinate system, the second Piola–Kirchhoff stress $\tilde{\mathbf{S}}$ is related to the Green–Lagrange strain $\tilde{\mathbf{E}}$ through the damage elasticity constitutive tensor $\tilde{\mathbf{C}}$ as

$$\begin{Bmatrix} \tilde{S}_{11} \\ \tilde{S}_{22} \\ \tilde{S}_{12} \end{Bmatrix} = \tilde{\mathbf{C}} \begin{Bmatrix} \tilde{E}_{11} - \tilde{E}^p_{11} \\ \tilde{E}_{22} - \tilde{E}^p_{22} \\ \tilde{E}_{12} \end{Bmatrix} \tag{7}$$

where $\tilde{E}^p_{11}$ and $\tilde{E}^p_{22}$ are the so-called permanent strains. The constitutive tensor $\tilde{\mathbf{C}}$ models a stress–strain response of an orthotropic material and may be expressed as

$$\tilde{\mathbf{C}} = \frac{1}{1-\nu_{21}\nu_{12}} \begin{bmatrix} E_1(1-D_{11}) & \nu_{21}E_1\sqrt{(1-D_{11})(1-D_{22})} & 0 \\ \nu_{12}E_2\sqrt{(1-D_{11})(1-D_{22})} & E_2(1-D_{22}) & 0 \\ 0 & 0 & G_{12}(1-D_{12}) \end{bmatrix} \tag{8}$$

where ν's are the Poisson ratios, E_1 and E_2 are the Young's moduli in the fiber and matrix directions, respectively, G_{12} is the shear modulus, and D_{11}, D_{22}, and D_{12} are the corresponding damage indices.

The damage indices D_{ij} are expressed as

$$D_{ij} = d^{\mathrm{t}}_{ij} + d^{\mathrm{c}}_{ij} \tag{9}$$

where d^{t}_{ij} and d^{c}_{ij} are the corresponding damage variables with the superscripts "t" and "c" used to distinguish between tensile and compressive damage modes. For the case of high-cycle fatigue, assuming no damage growth within the cycle, the evolution law for the damage variables is defined in terms of damage-growth-rate per cycle as

$$\begin{cases} \dfrac{d(d^{\mathrm{t}}_{ii})}{dN} = c_1[1+(d^{\mathrm{t}}_{ii})^2+D^2_{12}]\Sigma_{ii}\exp\left(-c_2\dfrac{d^{\mathrm{t}}_{ii}}{\sqrt{\Sigma_{ii}}(1+(d^{\mathrm{c}}_{ii})^2+D^2_{12})}\right)+c_3 d^{\mathrm{t}}_{ii}\Sigma^2_{ii} \\ \qquad \left[1+\dfrac{d^{\mathrm{c}}_{ii}\exp(c_8\sqrt{d^{\mathrm{c}}_{ii}})}{1+\exp(-c_5(\Sigma_{ii}-c_7))}\right]\times[1+\exp(c_5(\Sigma_{ii}-c_4))], \quad \text{if} \quad \tilde{S}_{ii}\geq 0 \\ \dfrac{d(d^{\mathrm{c}}_{ii})}{dN} = \{c_1[1+(d^{\mathrm{c}}_{ii})^2+D^2_{12}]\Sigma_{ii}\exp\left(-c_2\dfrac{d^{\mathrm{c}}_{ii}}{\sqrt{\Sigma_{ii}}(1+(d^{\mathrm{t}}_{ii})^2+D^2_{12})}\right)\}^{1+2\exp(-c_6 d^{\mathrm{t}}_{ii}-D_{12})} \\ \quad +c_3 d^{\mathrm{c}}_{ii}\Sigma^2_{ii}\left[1+\dfrac{d^{\mathrm{t}}_{ii}\exp(c_8\sqrt{d^{\mathrm{t}}_{ii}})}{1+\exp(-c_5(\Sigma_{ii}-c_7))}\right][1+\exp(\dfrac{c_5}{3}(\Sigma_{ii}-c_4))], \quad \text{if} \quad \tilde{S}_{ii}<0 \\ \dfrac{d(d^{\mathrm{t}}_{12})}{dN} = c_1[1+(d^{\mathrm{c}}_{12})^2]\Sigma_{12}\exp\left(-c_2\dfrac{d^{\mathrm{t}}_{12}}{2\sqrt{\Sigma_{12}}(1+(d^{\mathrm{c}}_{12})^2)}\right), \quad \text{if} \quad \tilde{S}_{12}\geq 0 \\ \dfrac{d(d^{\mathrm{c}}_{12})}{dN} = c_1[1+(d^{\mathrm{t}}_{12})^2]\Sigma_{12}\exp\left(-c_2\dfrac{d^{\mathrm{c}}_{12}}{2\sqrt{\Sigma_{12}}(1+(d^{\mathrm{t}}_{12})^2)}\right), \quad \text{if} \quad \tilde{S}_{12}<0 \end{cases} \tag{10}$$

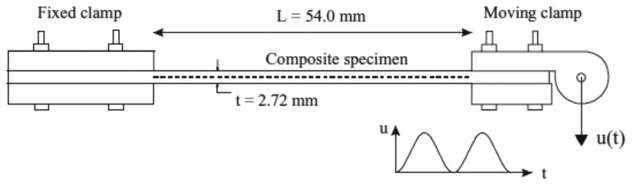

Fig. 2 Setup of the bending-fatigue test of a cantilever composite plate taken from Ref. [13]

Table 1 Material properties of glass fabric/epoxy lamina (R420/LY556)

Longitudinal modulus, E_1 (GPa)	24.57
Transverse modulus, E_2 (GPa)	23.94
Shear modulus, G_{12} (GPa)	4.83
Major Poisson's ratio, ν_{12}	0.153
Longitudinal tensile strength, X_t (MPa)	390.7
Longitudinal compressive strength, X_c (MPa)	345.1
Transverse tensile strength, Y_t (MPa)	390.7
Transverse compressive strength, Y_t (MPa)	345.1
Shear strength, Z (MPa)	100.6

Table 2 Fatigue-damage model parameters of the test specimen

C_1	c_2	c_3	c_4	c_5	c_6	c_7	c_8	c_9
0.003	30.0	3.5×10^{-6}	0.85	93.0	0	0	0	0.6

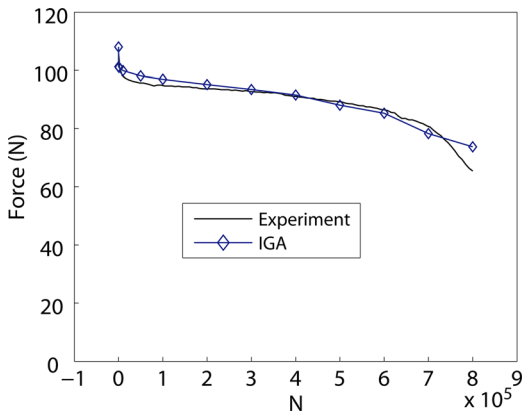

Fig. 3 Plot of the vertical force at the right clamp versus cycle number. Comparison of the IGA fatigue-damage simulation with experimental data.

where N denotes the cycle number, c's are the lamina-level material constants, and no summation on the repeated index i is assumed. The above damage-growth-rate equations also depend on the fatigue failure indices, denoted by Σ_{11}, Σ_{22}, and Σ_{12} and given by

$$\Sigma_{ij} = \frac{\Sigma_{ij}^{2D}}{1 + (\Sigma_{ij}^{2D} - \Sigma_{ij}^{1D})} \, (i,j = 1,2) \tag{11}$$

Equation (11) "blends" the indices for the decoupled longitudinal, transverse, and shear failure modes ($\Sigma_{ij^{1D}}{}'$s), and the indices based on the Tsai–Wu failure surface ($\Sigma'_{ij^{2D}}$s) [36]. The first set of fatigue failure indices is defined as follows:

$$\begin{cases} \Sigma_{11}^{1D} = \dfrac{\tilde{S}_{11}}{(1 - D_{11})X} \text{ where } X = \begin{cases} X_t & \tilde{S}_{11} \geq 0 \\ X_c & \tilde{S}_{11} < 0 \end{cases} \\ \Sigma_{22}^{1D} = \dfrac{\tilde{S}_{22}}{(1 - D_{22})Y} \text{ where } Y = \begin{cases} Y_t & \tilde{S}_{22} \geq 0 \\ Y_c & \tilde{S}_{22} < 0 \end{cases} \\ \Sigma_{12}^{1D} = \dfrac{|\tilde{S}_{12}|}{(1 - D_{12})Z} \end{cases} \tag{12}$$

where X is the longitudinal normal strength, Y is the transverse normal strength, Z_l is the shear strength, and subscripts "t" and "c" are used to distinguish between tensile and compressive action. The second set of indices is defined implicitly as

$$\left(\frac{1}{X_t} - \frac{1}{X_c}\right)\frac{\tilde{S}_{11}}{\Sigma_{11}^{2D}(1 - D_{11})} + \left(\frac{1}{Y_t} - \frac{1}{Y_c}\right)\frac{\tilde{S}_{22}}{1 - D_{22}} + \frac{1}{X_t X_c}\left(\frac{\tilde{S}_{11}}{\Sigma_{11}^{2D}(1 - D_{11})}\right)^2 + \frac{1}{Y_t Y_c}\left(\frac{\tilde{S}_{22}}{1 - D_{22}}\right)^2 + \frac{1}{Z^2}\left(\frac{\tilde{S}_{12}}{1 - D_{12}}\right)^2 = 1 \tag{13}$$

$$\left(\frac{1}{X_t} - \frac{1}{X_c}\right)\frac{\tilde{S}_{11}}{1 - D_{11}} + \left(\frac{1}{Y_t} - \frac{1}{Y_c}\right)\frac{\tilde{S}_{22}}{\Sigma_{22}^{2D}(1 - D_{22})} + \frac{1}{X_t X_c}\left(\frac{\tilde{S}_{11}}{1 - D_{11}}\right)^2 + \frac{1}{Y_t Y_c}\left(\frac{\tilde{S}_{22}}{\Sigma_{22}^{2D}(1 - D_{22})}\right)^2 + \frac{1}{Z^2}\left(\frac{\tilde{S}_{12}}{1 - D_{12}}\right)^2 = 1 \tag{14}$$

$$\left(\frac{1}{X_t} - \frac{1}{X_c}\right)\frac{\tilde{S}_{11}}{1 - D_{11}} + \left(\frac{1}{Y_t} - \frac{1}{Y_c}\right)\frac{\tilde{S}_{22}}{1 - D_{22}} + \frac{1}{X_t X_c}\left(\frac{\tilde{S}_{11}}{1 - D_{11}}\right)^2 + \frac{1}{Y_t Y_c}\left(\frac{\tilde{S}_{22}}{1 - D_{22}}\right)^2 + \frac{1}{Z^2}\left(\frac{\tilde{S}_{12}}{\Sigma_{12}^{2D}(1 - D_{12})}\right)^2 = 1 \tag{15}$$

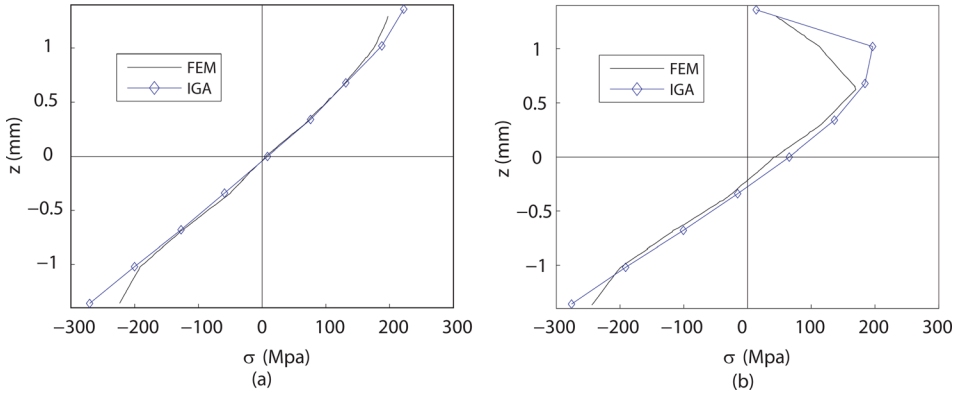

Fig. 4 Stress redistribution at the clamped cross section at cycle: (*a*) $N = 8{,}000$ and (*b*) $N = 650{,}000$. Comparison of the IGA results with the finite-element simulation data.

Table 3 Blade cross section geometry data for the CX-100 blade

Radial distance (m)	Chord length (m)	Twist angle (deg)	Airfoil type
0.200	0.356	29.6	Cylinder
0.600	0.338	24.8	Cylinder
1.000	0.569	20.8	Cylinder
1.400	0.860	17.5	NREL S821
1.800	1.033	14.7	NREL S821
2.200	0.969	12.4	NREL S821
3.200	0.833	8.3	NREL S821
4.200	0.705	5.8	NREL S819
5.200	0.582	4.0	NREL S819
6.200	0.463	2.7	NREL S819
7.200	0.346	1.4	NREL S819
8.200	0.232	0.4	NREL S819
9.000	0.120	0.0	NREL S820

Finally, the accumulation of permanent strains (see Eq. (7)) is attributed to the growth of shear damage, and the corresponding growth law is stated as

$$\frac{d\tilde{E}^p_{ii}}{dN} = \begin{cases} c_9 \tilde{E}_{ii} \dfrac{dD_{12}}{dN} & \text{if} \quad \tilde{S}_{ii} \geq 0 \\ 0 & \text{if} \quad \tilde{S}_{ii} < 0 \end{cases} (i = 1, 2) \tag{16}$$

where no summation on the repeated index i is assumed, and c_9 is an additional material parameter.

In the numerical implementation of the shell model, every ply has its own set of spatially varying damage indices that go in the definition of the constitutive tensor given by Eq. (8). The damage indices and constitutive tensor are defined in each ply and at every quadrature point on the shell surface. The computation of extensional, coupling, and bending stiffnesses, which makes use of the through-thickness homogenization procedure outlined in the previous section, now makes use of the constitutive tensor with built-in damage information, as per Eq. (8).

3.1 Numerical Validation of the Fatigue Damage Model. The above fatigue-damage model is validated using a bending-fatigue test of a cantilever composite plate carried out in Ref. [13]. The experimental setup and specimen geometry are shown in Fig. 2. Both sides of the specimen are clamped, however, the right clamp is moving with a prescribed velocity as shown in the figure. The specimen width is 30 mm. The material used is a glass fabric/epoxy composite (R420/LY556), where the fiber is a Roviglass R420 plain woven glass fabric and the epoxy is Araldite LY 556. The stacking sequence is $[0\ \text{deg}]_8$, where "0" is aligned with the loading direction. The material properties of the composite lamina are listed in Table 1. The specimen is manufactured by the resin-transfer-molding technique with the total thickness after curing of 2.72 mm.

The fatigue model coefficients, also taken from Ref. [13], are listed in Table 2. The problem is discretized using a mesh of 10×5 quadratic NURBS elements. The damage evolution equations are integrated using an explicit Euler method. To enhance the computational efficiency, a cycle jump technique is employed,

Table 4 Lamina properties of the materials employed in the CX-100 blade

Material name	E_1 (GPa)	E_2 (GPa)	G_{12} (GPa)	ν_{12}	ρ (kg/m^3)
Gel coat	3.44	3.44	1.38	0.30	1,235
Fill epoxy	2.41	2.41	0.96	0.30	1,154
Fiberglass	7.58	7.58	4.00	0.30	1,678
End-grain balsa	0.12	0.12	0.02	0.30	230
DBM1708 (±45 deg fiberglass)	9.58	9.58	6.89	0.39	1,814
DBM1208 (±45 deg fiberglass)	9.58	9.58	6.89	0.39	1,814
C520 (0 deg fiberglass)	37.30	7.60	6.89	0.31	1,874
Zero degree carbon, 500 gsm	105.40	6.82	3.32	0.28	1,480
Carbon-fiberglass triaxial fabric	84.10	8.76	4.38	0.21	1,560

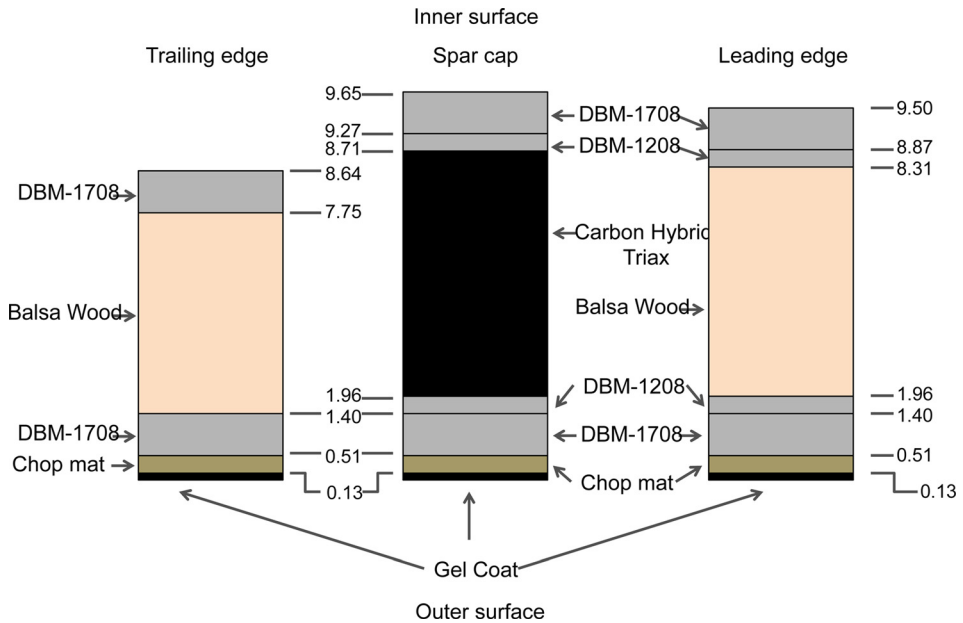

Fig. 5 Layup of the trailing edge, leading edge, and spar cap

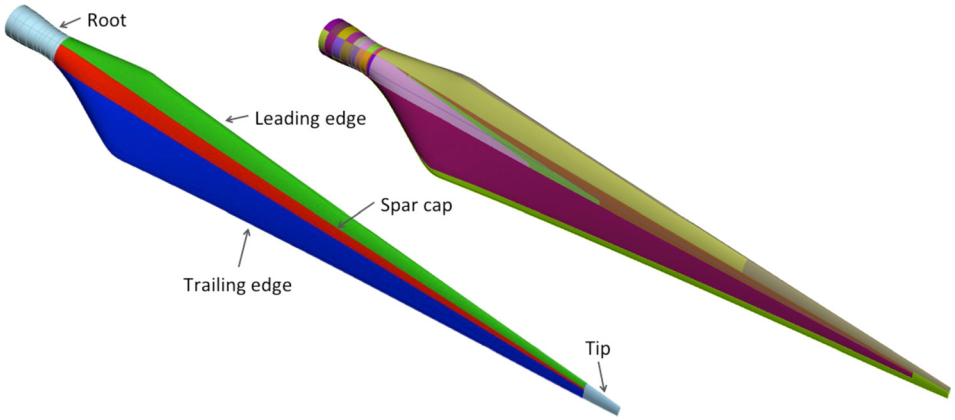

Fig. 6 Left: five primary sections of the CX-100 blade and right: 32 distinct material zones of the CX-100 blade

where the stress state that drives the damage model is obtained by solving the Kirchhoff–Love shell equations for every *NJUMP* cycles of the damage evolution, where *NJUMP* is a user-controlled parameter. The same cycle jump technique is used in the computations involving a full-scale wind-turbine blade presented in the next section.

Remark. Although a constant value is employed in the present work, *NJUMP* can be selected adaptively by ensuring that the damage index does not increase by more than *N%* for a given sampled stress state. (*N* can be chosen in a conservative fashion to minimize the error). Although the damage evolution equations are very complicated to lend themselves to simple analysis, one does

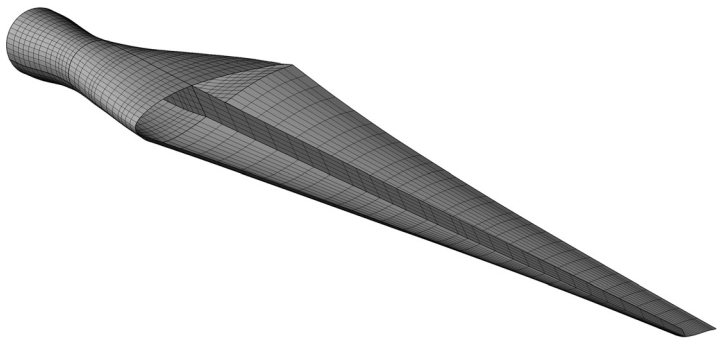

Fig. 7 NURBS mesh of the CX-100 blade. A few top-surface patches are removed to show the shear web attachment and mesh.

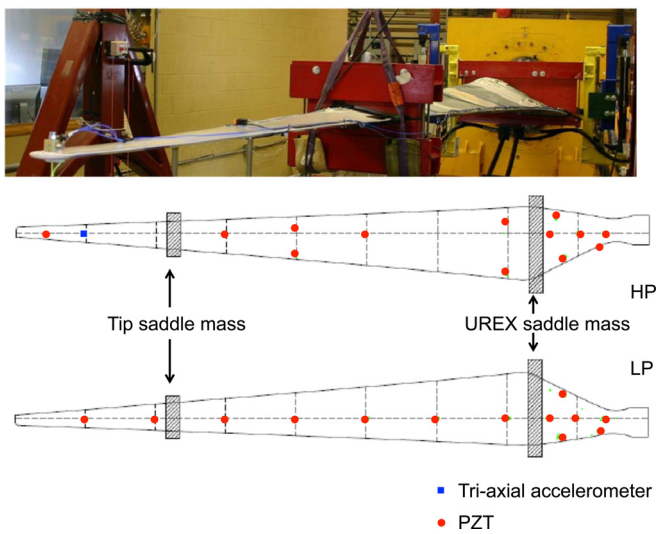

Fig. 8 Blade fatigue test setup and sensor layout. Square symbols gives the location of the accelerometer providing dynamic acceleration data for displacement amplitude and fatigue-model parameter calibration.

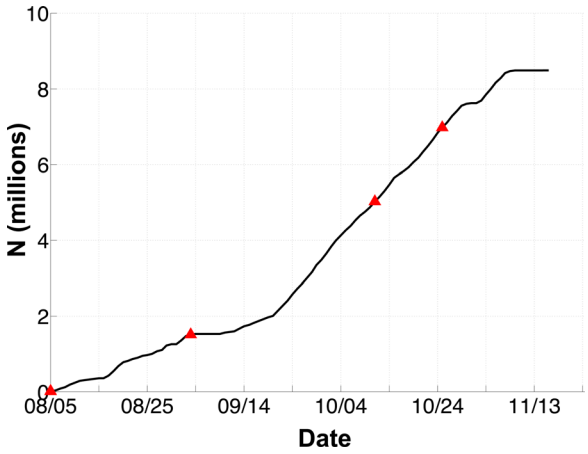

Fig. 9 Fatigue cycle count versus date. Triangular symbols indicate calibration points for fatigue-damage simulations.

identify regions of rapid material degradation in the initial and final stages of fatigue loading. Using this strategy, NJUMP will automatically be selected to take smaller values in these regions.

Figure 3 shows maximum during the cycle vertical reaction force at the right clamp as a function of cycle number. The predicted reaction-force history compares well with the experimental data from Ref. [13]. Note a sharp decline in the initial stiffness in the first few hundred loading cycles followed by a gradual stiffness reduction. Figure 4 shows the distribution of longitudinal stress along the plate thickness at the stationary clamped cross section. Early on, after 8,000 cycles, the stress follows an expected near-linear profile. After about 650,000 cycles, the stress redistributes over the cross section due to damage growth in the upper plies. Damage first occurs and grows on the tensile side, which moves the neutral axis down toward the compressive side. The IGA results are compared with the finite-element simulation data from Ref. [13]. Although the latter assumed richer through-thickness kinematics compared to the present Kirchhoff–Love shell theory, the overall stress comparison is quite good.

4 Fatigue Damage Simulation of a Full-Scale CX-100 Wind-Turbine Blade Driven by Test Data

In this section, we show the deployment of our DDDAS framework using data from a fatigue test of a full-scale wind-turbine blade. We describe the blade geometry and material composition, the fatigue test setup and sensors employed, and the computational procedure for fatigue-damage identification and prediction that involves dynamic computational model updating based on sensor and measurement data collected during the test.

4.1 Blade Structure and Its IGA Model. We use a Sandia CX-100 conventional carbon-spar wind-turbine blade design [33,37,38], which is based on the ERS-100 blade [38], but with a substantially reduced spar cap. The blade surface geometry definition is provided in Table 3. Up to a 1-m station from the root, the blade has a circular cross section. At a 1.4-m station, the blade transitions into the NREL S821 airfoil with a twist angle of 17.5 deg. At a 4.2-m station, the blade blends into the NREL S819 airfoil, which is used almost all the way to the tip where the NREL S820 airfoil is placed. The airfoils are lofted along the blade axis direction to produce a NURBS blade surface.

The blade material composition is as follows. The blade surface comprises five primary zones: leading edge, trailing edge, root, spar cap, and shear web. The zones are shown in Fig. 6. Each zone is made up of a multilayer composite layup. The different materials used for the layup are summarized in Table 4. The root area has several layers of fiberglass plies to strengthen the region where the blade is mounted on the hub flange. The leading and trailing edge zones have a similar layup. Both include an outer gel coat and fiberglass layers, with the total thickness of 0.51 mm, as well as additional layers of fiberglass material DBM-1708, 0.89 mm each, and one 6.35 mm layer of balsa wood. Balsa wood is only present in the core section of the blade and not on the edges. The leading edge zone has additional layers of fiberglass material DBM-1208, with a total thickness of 0.56 mm, located between DBM-1708 and balsa core. The layup of the core regions of the trailing and leading edge zones is shown in Fig. 5. The spar-cap zone has a nonuniform thickness distribution, ranging from 5.79 mm to 9.65 mm, due to the decreasing number of carbon fiber laminate layers (from seven to three) along the blade length. The spar-cap layup is also shown in Fig. 5 and has the thickest carbon fiber layer. The shear web, which is designed to carry most of the surface loads, has a C-shape structure containing four layers of DBM-1708 fiberglass, 0.74 mm each, and 9.53 mm of balsa wood core. The balsa wood layer is terminated in the tip zone. As a result, the tip region is only comprised of one layer of gel coat and several layers of fiberglass material. This layout leads to 32 zones with constant total thickness and unique laminate stacking. All 32 zones are identified on the blade surface and are shown in Fig. 6. The blade mesh chosen for this study has 4,647 quadratic NURBS elements and is shown in Fig. 7, where the top surface of the blade is removed to show the placement of the shear web. This mesh resolution produced excellent results in a validation study through eigenfrequency analysis reported in Ref. [33] and is felt to be adequate for the present application.

4.2 Blade Fatigue-Test Setup and Sensor Layout. The CX-100 blade was fatigue loaded until failure using a hydraulic displacement excitation technique at the National Wind Technology Center (NWTC) in Golden, CO as a part of the Los Alamos National Laboratory Wind Turbine Program [22,24,25]. During the test, the blade was clamped at the root and turned such that the high-pressure side was facing up, and, at a 7-m station, the local chord was parallel to the laboratory floor (see Fig. 8). The blade was driven at the natural frequency of the first flapwise bending mode, which is 1.82 Hz. The cyclic load was applied at a 1.6-m station using universal resonance excitation hydraulic actuators. The applied-force magnitude during the test was adjusted by changing the stroke of the hydraulic actuators. To amplify the blade response, an additional mass of 164.65 kg was placed at a 6.7-m station. Figure 9 shows the fatigue cycle count versus date. The fatigue test lasted from August 5, 2011 to November 13, 2011, until a fatigue-induced crack formed in the blade root region after about 8.0 M loading cycles.

The CX-100 blade was equipped with a number of sensors for both active and passive sensing applications [22–25,39–41]. All the sensors were located on the blade exterior with most of them concentrated near the root where fatigue failure was expected to occur (and, indeed, occurred). The primary sensors employed were piezoelectric transducers (PZTs), in particular, WASP-1, Metis-1, and LASER. Also, several macrofiber-composite sensors were used as a backup sensor. The layout of PZT sensors on both high- and low-pressure sides of the blade is shown in Fig. 8. Traditional accelerometers that record acceleration during 10-s intervals at a sampling rate of 1.6 kHz were also installed at several locations on the blade surface. Additional devices included strain gauges for strain measurements and moment calibration, and temperature sensors. A rich dataset from these sensors was collected and analyzed in Refs. [22–25]. In particular, SHM techniques for fatigue crack detection and their comparison were discussed at length in Ref. [25]. In the present work, we mainly focus on the accelerometer data to steer the fatigue-damage computations, which are presented in the following section.

4.3 Blade Fatigue Simulation Driven by Test Data. The dynamic data collected during the CX-100 blade fatigue test is

employed for blade fatigue-damage simulation. Although, ideally, the computation would be executed concurrently with the fatigue test, here the measurements from the fatigue test are employed as historic or archival data used to steer the fatigue-damage computation. To carry out the simulation, the IGA model of the CX-100 blade is placed in the same orientation as the test specimen and is also clamped at the root. A time-periodic vertical displacement with frequency of 1.82 Hz is applied at a 1.6-m station to mimic the hydraulic-system forcing. The effect of extra mass of 164.65 kg added to the 6.7-m station is achieved by locally increasing the blade material density in this region. The dynamic sensor data are employed to simultaneously calibrate the magnitude of the applied displacement loading, as well as to obtain a good estimate of the input parameters of the fatigue-damage model. To this end, we devise two DDDAS loops—the *inner loop* responsible for displacement forcing amplitude calibration and the *outer loop* responsible for simulation of damage growth and calibration of the associated material constants. The flowchart for each of the two DDDAS loops is shown in Fig. 10. The amplitude of the applied displacement used to actuate the blade is calibrated at four points during the fatigue test, corresponding to cycle number 0 M, 1.5 M, 5 M, and 7 M (see Fig. 9). At each one of these points, a dynamic simulation consisting of a few flapping cycle is performed with material parameters corresponding to the blade damage state at that cycle, as predicted by the fatigue-damage model. The prescribed displacement amplitude is adjusted until

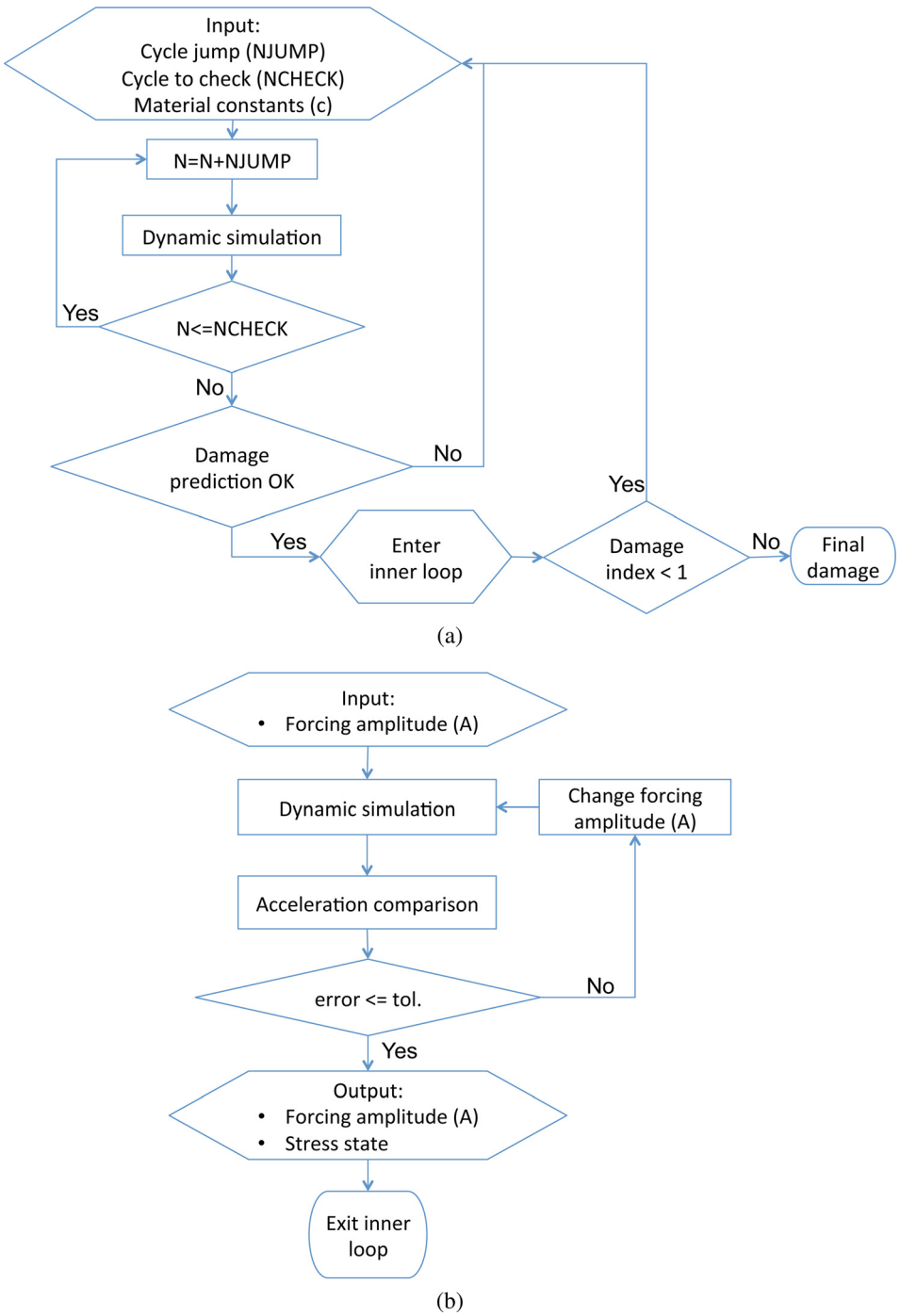

Fig. 10 (*a*) Flowchart of the outer DDDAS loop responsible for fatigue-damage prediction and model parameter calibration and (*b*) flowchart of the inner DDDAS loop responsible for applied displacement amplitude calibration

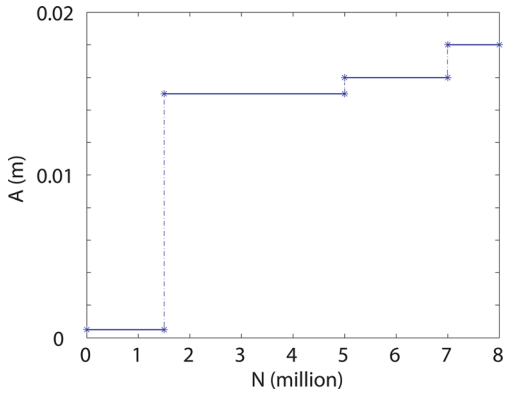

Fig. 11 Amplitude (*A*) of applied displacement forcing as a function of cycle number (*N*)

the acceleration time history at location 8.05 m predicted by the simulation matched that measured by the accelerometer placed in this location (see Fig. 8). Figure 11 shows the calibrated displacement forcing amplitude as a function of cycle number, while Fig. 12 shows the degree to which we are able to match the predicted and measured accelerations. The acceleration data comparison is presented in the time and frequency domains. Note that both the displacement and acceleration amplitudes are increasing with cycle number.

The fatigue-damage model parameters are summarized in Table 5. We start with the values close to those used for the test specimen in Sec. 3.1 and adjust the model parameters c_1 and c_3 to properly reflect the current damage state of the structure at the same four calibration points during the fatigue test. Figure 13 shows the evolution of c_1 and c_3 as a function of cycle number. This evolution gives the predicted blade fatigue life of about 8 M cycle, which is in good agreement with the test data.

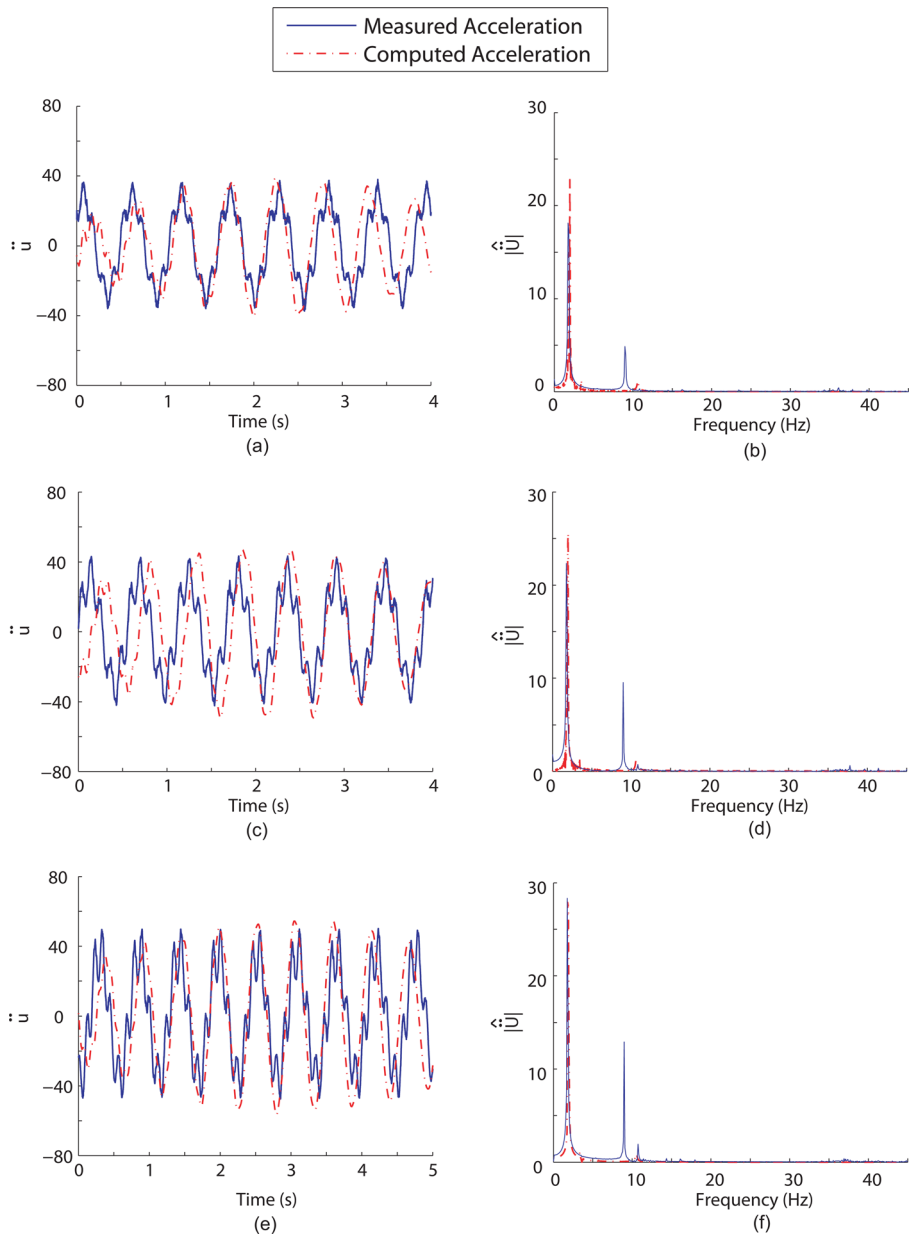

Fig. 12 Acceleration data comparison between the fatigue test and simulation at four calibration points. Left: time domain comparison and right: frequency domain comparison.

Table 5 Damage model parameters of CX-100 blade employed in the computations

Cycle	c_1	c_2	c_3	c_4	c_5	c_6	c_7	c_8	c_9
≤1.5 M	4×10^{-6}	30.0	2.0×10^{-6}	0.8	80.0	0	0	0	0
1.5–5.0 M	4×10^{-6}	30.0	2.0×10^{-6}	0.8	80.0	0	0	0	0
5.0–7.0 M	1.6×10^{-4}	30.0	4.0×10^{-5}	0.8	80.0	0	0	0	0
7.0–8.0 M	4×10^{-4}	30.0	1.0×10^{-4}	0.8	80.0	0	0	0	0

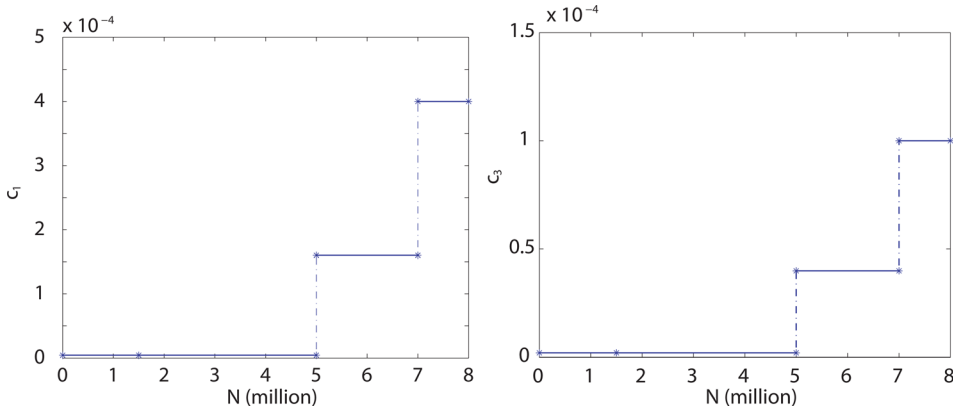

Fig. 13 Damage model material parameters c_1 (left) and c_3 (right) plotted versus cycle number

Remark. The four points chosen for calibration correspond to the points in the test where the acceleration measurements showed the biggest change. In principle, one is free to choose as many calibration points as necessary for good accuracy of the fatigue-damage prediction.

Figures 14 and 15 show the evolution of damage index D_1 (i.e., fiber direction) in the DBM plies. (Note that two different scales are employed for the two figures.) For the first 1.5 M cycles, damage grows faster in the blade midspan. After 1.5 M cycles, damage begins to concentrate and grow in the root section. This is likely due to a significant increase in the displacement forcing amplitude after 1.5 M cycles (see Fig. 11). Closer to 8 M cycles, a part of the root section is fully damaged, and the damage location is in excellent agreement with that of the crack observed on the blade surface during the fatigue test. (See Fig. 16 for a visual comparison of the fatigue-test and simulation results.)

5 Conclusions and Future Work

A novel framework for fatigue-damage modeling in large-scale laminated composite structures is proposed where the simulations are infused with dynamic sensor and measurement data to increase the physical realism of the simulations and enhance their predictive power. The proposed framework is deployed in the context of a fatigue test of a full-scale wind-turbine blade structure, and good results are obtained for the prediction of damage zone

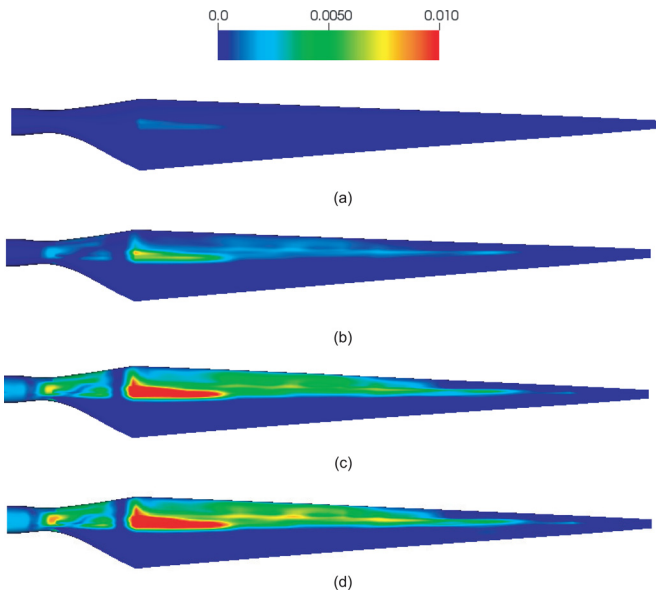

Fig. 14 Progression of damage index D_1 up to 1.5 M cycles in a DBM layer: (*a*) cycle $N = 10{,}000$, (*b*) cycle $N = 100{,}000$, (*c*) cycle $N = 1{,}000{,}000$, and (*d*) cycle $N = 1{,}500{,}000$

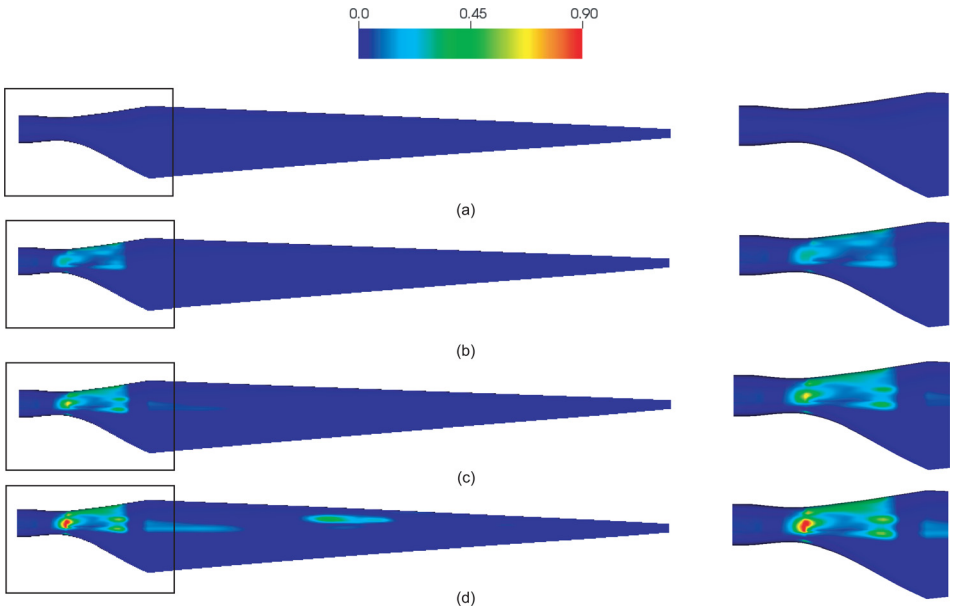

Fig. 15 Progression of damage index D_1 from 1.5 M to 8.0 M cycles in a DBM layer: (*a*) cycle $N = 1{,}500{,}000$, (*b*) cycle $N = 5{,}000{,}000$, (*c*) cycle $N = 7{,}000{,}000$, and (*d*) cycle $N = 8{,}000{,}000$

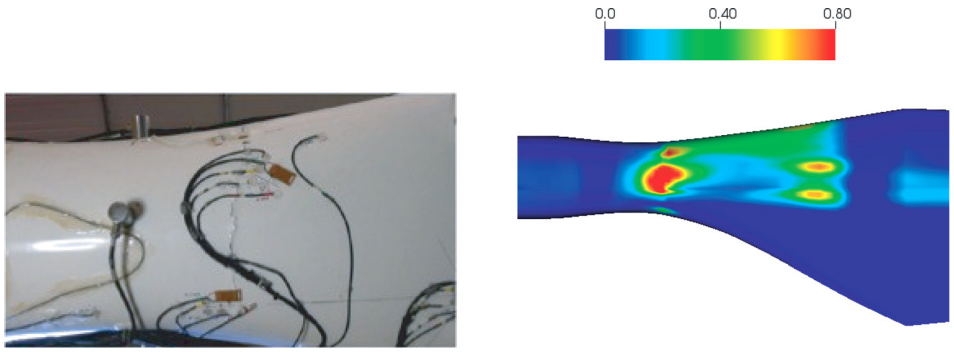

Fig. 16 Visual comparison of the fatigue-test and simulation results. Location and shape of the damage zone in a DBM layer near the root are in very good agreement with the location and orientation of the crack observed in the fatigue test.

formation and evolution, eventually leading to blade failure. The fatigue model, adapted from Refs. [12] and [13], is based on continuum damage mechanics and residual stiffness approaches and is well suited for the implementation with a multilayer composite thin shell. While each of the framework constituents was proposed earlier and studied in the context of other applications, the main novelty of the present contribution is in the synthesis of the modeling constituents and their integration with dynamic measurement data. In addition, a successful application of the fatigue-damage model from Refs. [12] and [13] to a full-scale laminated composite structure is presented for the first time.

It is recognized that the current framework accommodates only thin shells. In the thicker shell case, a Reissner–Mindlin type shell theory with transverse shearing deformations needs to be considered, necessitating the use of rotational degrees-of-freedom [16]. Furthermore, no delamination modeling is considered in the present work, which is an important failure mode in laminated composites. We plan to introduce these and other improvements in the modeling in order to handle a larger class of composite structures and loading scenarios.

To further increase the predictive power of the proposed framework, a more rigorous parameter estimation technique for the damage-model constants needs to be employed. Our current efforts are focused on formulating an optimization strategy based on a derivative-free approach [42], which relies on surrogate functions (or approximations) for improved efficiency of the optimization algorithm.

The present DDDAS framework requires occasional dynamic simulations to sample the stress state in the structure, which, in turn, drives fatigue-damage evolution. Although standalone nonlinear structural dynamic simulations are performed in this work as part of fatigue-damage prediction, in general, more complex models may be considered. We are presently extending the framework to incorporate 3D coupled fluid–structure interaction, which predicts the structure stress state under realistic aerodynamic and hydrodynamic loading, and, as a result, presents a pathway to predicting useful life span of structures subjected to such loads. In this case, the laboratory fatigue tests may be employed for the calibration of damage model parameters for the simulations corresponding to actual structure operating conditions.

Acknowledgment

Y.B., A.K., and F.L. were supported through AFOSR Award No. FA9550-12-1-0005. X.D. was supported through AFOSR Award No. FA9550-12-1-0046. S.T. was funded by the

Department of Energy through a Laboratory Research and Development (LDRD) Program. M.T. was funded by the Leading Foreign Research Institute Recruitment Program through the National Research Foundation of Korea funded by the Ministry of Education, Science and Technology (2011-0030065). This support is gratefully acknowledged.

References

[1] Darema, F., 2004, "Dynamic Data Driven Applications Systems: A New Paradigm for Application Simulations and Measurements," 4th International Conference on Computational Science (ICCS'04), Krakow, Poland, June 6–9, pp. 662–669.

[2] Bazilevs, Y., Marsden, A., di Scalea, F. L., Majumdar, A., and Tatineni, M., 2012, "Toward a Computational Steering Framework for Large-Scale Composite Structures Based on Continually and Dynamically Injected Sensor Data," Procedia Comput. Sci., **9**, pp. 1149–1158.

[3] Andrianarison, O., and Ohayon, R., 2006, "Reduced Models for Modal Analysis of Fluid–Structure Systems Taking Into Account Compressibility and Gravity Effects," Comput. Methods Appl. Mech. Eng., **195**(41), pp. 5656–5672.

[4] Ohayon, R., 2001, "Reduced Symmetric Models for Modal Analysis of Internal Structural-Acoustic and Hydroelastic-Sloshing Systems," Comput. Methods Appl. Mech. Eng., **190**(24–25), pp. 3009–3019.

[5] Degrieck, J., and Paepegem, W. V., 2001, "Fatigue Damage Modelling of Fiber-Reinforced Composite Materials: Review," ASME Appl. Mech. Rev., **54**(4), pp. 279–300.

[6] Fong, J. T., 1982, "What is Fatigue Damage," *Damage in Composite Materials*, American Society for Testing and Materials, West Conshohocken, PA.

[7] Deng, X., Korobenko, A., Yan, J., and Bazilevs, Y., 2015, "Isogeometric Analysis of Continuum Damage in Rotation-Free Composite Shells," Comput. Methods Appl. Mech. Eng., **284**, pp. 349–372.

[8] Raghavan, P., Li, S., and Ghosh, S., 2004, "Two Scale Response and Damage Modeling of Composite Materials," Finite Elem. Anal. Des., **40**(12), pp. 1619–1640.

[9] Swaminathan, S., Ghosh, S., and Pagano, N. J., 2006, "Statistically Equivalent Representative Volume Elements for Composite Microstructures. Part I: Without Damage," J. Compos. Mater., **40**(7), pp. 583–604.

[10] Swaminathan, S., and Ghosh, S., 2006, "Statistically Equivalent Representative Volume Elements for Composite Microstructures. Part II: With Evolving Damage," J. Compos. Mater., **40**(7), pp. 605–621.

[11] Sendeckyj, G. P., 1990, "Life Prediction for Resin-Matrix Composite Materials," *Fatigue of Composite Materials*, Elsevier, New York, Chap. 10.

[12] Paepegem, W. V., and Degrieck, J., 2004, "Simulating In-Plane Fatigue Damage in Woven Glass Fibre-Reinforced Composites Subject to Fully Reversed Cyclic Loading," Fatigue Fract. Eng. Mater. Struct., **27**(12), pp. 1197–1208.

[13] Paepegem, W. V., and Degrieck, J., 2002, "A New Coupled Approach of Residual Stiffness and Strength for Fatigue of Fiber-Reinforced Composites," Int. J. Fatigue, **24**(7), pp. 747–762.

[14] Kiendl, J., Bletzinger, K.-U., Linhard, J., and Wüchner, R., 2009, "Isogeometric Shell Analysis With Kirchhoff–Love Elements," Comput. Methods Appl. Mech. Eng., **198**(49), pp. 3902–3914.

[15] Kiendl, J., Bazilevs, Y., Hsu, M.-C., Wüchner, R., and Bletzinger, K.-U., 2010, "The Bending Strip Method for Isogeometric Analysis of Kirchhoff–Love Shell Structures Comprised of Multiple Patches," Comput. Methods Appl. Mech. Eng., **199**(37), pp. 2403–2416.

[16] Benson, D. J., Bazilevs, Y., Hsu, M.-C., and Hughes, T. J. R., 2010, "Isogeometric Shell Analysis: The Reissner–Mindlin Shell," Comput. Methods Appl. Mech. Eng., **199**(5–8), pp. 276–289.

[17] Benson, D. J., Bazilevs, Y., Hsu, M.-C., and Hughes, T. J. R., 2011, "A Large Deformation, Rotation-Free, Isogeometric Shell," Comput. Methods Appl. Mech. Eng., **200**(13–16), pp. 1367–1378.

[18] Benson, D. J., Hartmann, S., Bazilevs, Y., Hsu, M.-C., and Hughes, T., 2013, "Blended Isogeometric Shells," Comput. Methods Appl. Mech. Eng., **255**, pp. 133–146.

[19] Echter, R., Oesterle, B., and Bischoff, M., 2013, "A Hierarchic Family of Isogeometric Shell Finite Elements," Comput. Methods Appl. Mech. Eng., **254**, pp. 170–180.

[20] Bazilevs, Y., Hsu, M.-C., Kiendl, J., Wüchner, R., and Bletzinger, K.-U., 2011, "3D Simulation of Wind Turbine Rotors at Full Scale. Part II: Fluid–Structure Interaction Modeling With Composite Blades," Int. J. Numer. Methods Fluids, **65**(1–3), pp. 236–253.

[21] Bazilevs, Y., Hsu, M.-C., Kiendl, J., and Benson, D. J., 2012, "A Computational Procedure for Prebending of Wind Turbine Blades," Int. J. Numer. Methods Eng., **89**(3), pp. 323–336.

[22] Farinholt, K., Taylor, S., Park, G., and Ammerman, C., 2012, "Full-Scale Fatigue Tests of CX-100 Wind Turbine Blades. Part I: Testing," Proc. SPIE, **8343**, p. 83430P.

[23] Taylor, S., Jeong, H., Jang, J., Park, G., Farinholt, K., Todd, M., and Ammerman, C., 2012, "Full-Scale Fatigue Tests of CX-100 Wind Turbine Blades. Part II: Analysis," Proc. SPIE, **8343**, p. 83430Q.

[24] Taylor, S., Farinholt, K., Jeong, H., Jang, J., Park, G., Todd, M., Farrar, C., and Ammerman, C., 2012, "Wind Turbine Blade Fatigue Tests: Lessons Learned and Application to SHM System Development," 6th European Workshop on Structural Health Monitoring, Dresden, Germany, July 3–6, pp. 1324–1334.

[25] Taylor, S., Park, G., Farinholt, K., and Todd, M., 2013, "Fatigue Crack Detection Performance Comparison in a Composite Wind Turbine Rotor Blade," Struct. Health Monit., **12**(3), pp. 252–262.

[26] Hughes, T. J. R., Cottrell, J. A., and Bazilevs, Y., 2005, "Isogeometric Analysis: CAD, Finite Elements, NURBS, Exact Geometry, and Mesh Refinement," Comput. Methods Appl. Mech. Eng., **194**(39–41), pp. 4135–4195.

[27] Cottrell, J. A., Hughes, T. J. R., and Bazilevs, Y., 2009, *Isogeometric Analysis: Toward Integration of CAD and FEA*, Wiley, Chichester, UK.

[28] Bazilevs, Y., da Veiga, L. B., Cottrell, J. A., Hughes, T. J. R., and Sangalli, G., 2006, "Isogeometric Analysis: Approximation, Stability and Error Estimates for *h*-Refined Meshes," Math. Models Methods Appl. Sci., **16**(7), pp. 1031–1090.

[29] Piegl, L., and Tiller, W., 1997, *The NURBS Book (Monographs in Visual Communication)*, 2nd ed., Springer, New York.

[30] Sederberg, T. W., Cardon, D., Finnigan, G., North, N., Zheng, J., and Lyche, T., 2004, "T-Spline Simplification and Local Refinement," ACM Trans. Graphics, **23**(3), pp. 276–283.

[31] Bazilevs, Y., Calo, V. M., Cottrell, J. A., Evans, J. A., Hughes, T. J. R., Lipton, S., Scott, M. A., and Sederberg, T. W., 2010, "Isogeometric Analysis Using T-Splines," Comput. Methods Appl. Mech. Eng., **199**(5–8), pp. 229–263.

[32] Bazilevs, Y., Hsu, M.-C., and Scott, M. A., 2012, "Isogeometric Fluid–Structure Interaction Analysis With Emphasis on Non-Matching Discretizations, and With Application to Wind Turbines," Comput. Methods Appl. Mech. Eng., **249–252**, pp. 28–41.

[33] Korobenko, A., Hsu, M.-C., Akkerman, I., Tippmann, J., and Bazilevs, Y., 2013, "Structural Mechanics Modeling and FSI Simulation of Wind Turbines," Math. Models Methods Appl. Sci., **23**(2), pp. 249–272.

[34] Reddy, J. N., 2004, *Mechanics of Laminated Composite Plates and Shells: Theory and Analysis*, 2nd ed., CRC Press, Boca Raton, FL.

[35] Chung, J., and Hulbert, G. M., 1993, "A Time Integration Algorithm for Structural Dynamics With Improved Numerical Dissipation: The Generalized-α Method," ASME J. Appl. Mech., **60**(2), pp. 371–375.

[36] Daniel, I. M., and Ishai, O., 2006, *Engineering Mechanics of Composite Materials*, Oxford University Press, New York.

[37] Zayas, J., and Johnson, W., 2008, "3X-100 Blade Field Test," Wind Energy Technology Department, Sandia National Laboratories, Albuquerque, NM, Report No. SAND2007-5138.

[38] Berry, D., and Ashwill, T., 2007, "Design of 9-Meter Carbon-Fiberglass Prototype Blades: CX-100 and TX-100," Sandia National Laboratories, Albuquerque, NM, Report No. SAND2007-0201.

[39] Tippmann, J., Zhu, P., and di Scalea, F. L., 2015, "Application of Damage Detection Methods Using Passive Reconstruction of Impulse Response Functions," Philos. Trans. R. Soc., A, **373**(2035), p. 20140070.

[40] Tippmann, J., and di Scalea, F. L., 2015, "Passive-Only Damage Detection by Reciprocity of Green's Functions Reconstructed From Diffuse Acoustic Fields With Application to Wind Turbine Blades," J. Intell. Mater. Syst. Struct., **26**, pp. 1251–1258.

[41] Tippmann, J., and di Scalea, F. L., 2014, "Experiments on a Wind Turbine Blade Testing: An Indication for Damage Using the Causal and Anti-Causal Green's Function Reconstructed From a Diffuse Field," Proc. SPIE, **9064**, p. 90641I.

[42] Booker, A. J., Dennis, J. E., Jr., Frank, P. D., Serafini, D. B., Torczon, V., and Trosset, M. W., 1999, "A Rigorous Framework for Optimization of Expensive Functions by Surrogates," Struct. Optim., **17**(1), pp. 1–13.